Research Article | Vol. 30, No. 8 / 11 Apr 2022 / Optics Express 13540
Optics EXPRESS

Algorithmic decoding of dense OAM signal constellations for optical communications in turbulence

JAIME A. ANGUITA[1,2,*] AND JAIME E. CISTERNAS[1,2]

[1] Universidad de los Andes, Chile
[2] Millennium Institute for Research in Optics (MIRO), Chile
[*] janguita@miuandes.cl

Abstract: We demonstrate an optical detection and decoding strategy to increase the information rate and spectral efficiency of free-space laser communication links affected by turbulence by means of dense orbital angular momentum (OAM) modulation. Using three candidate receiver architectures–based on a Shack-Hartmann sensor, a Mode Sorter, and a complex conjugate projection scheme as a base case–we demonstrate an algorithmic classification system based on the received OAM spectra produced by these architectures. This classification scheme allows low-error-rate data transmission in turbulence using 16-OAM, 32-OAM, and 64-OAM symbol constellations, with OAM states between −20 and 20. We evaluate and compare their performance under weak to strong atmospheric turbulence conditions using an accuracy metric and confusion matrices.

1. Introduction

The orbital angular momentum (OAM) of light has been under study for the past 30 years to establish its real potential to expand –among other fields– the aggregate capacity of free-space optical communications [1–5]. The high dimensionality that OAM could potentially offer to the transmission of information over unguided optical channels will be limited by the ability of the communication system to distinguish all distinct states employed to carry the information [6–10].

Because refractive-index fluctuations induced by atmospheric turbulence alter both the spatial phase and the amplitude of a beam, and given that OAM is a spatial property of light, random distortions are coupled to the very property one needs to determine. This coupling limits the capacity of a system based in OAM in an intrinsic way [7].

In any case, proper detection and estimation of the OAM requires that the full intensity distribution –the complete wave function for a single-photon system– be available to the optical processor. Partial detection of the beam's light will otherwise result in a further limited capacity to resolve the state [2]. Such optical processor must have knowledge of the beam's axis to properly project its field to an orthogonal basis and determine the carried OAM. If instead the processor only needs to classify the OAM within a discrete class of elements, the processor is required to be physically oriented to maximize distinguishability [11,12].

An undistorted beam carrying a single OAM state can be correctly classified or measured if it is perfectly aligned with the axis of the receiver. Any tilt or lateral misalignment will deliver a spread of OAM values [13,14], analogous to the partial rotation of an orthogonal basis. Thus, alignment of the system to the beam's axis is critical for achieving good OAM state discrimination. If this optical property is used for data transmission in terrestrial free-space optical links (or land to satellite), a fundamental requirement is knowing how well the OAM modes distorted by turbulence can be distinguished.

Symbol detection in optical communications demands a photon-efficient sensing of data symbols to effectively increase power and spectral efficiency. A high-dimensional modulation

#455425 https://doi.org/10.1364/OE.455425
Journal © 2022 Received 2 Feb 2022; revised 23 Mar 2022; accepted 23 Mar 2022; published 6 Apr 2022

Optics EXPRESS

system –i.e., using more than two states– is commonly designed using a set of orthogonal branches over which the signal is split [15]. This method, although widely used in radio-frequency communications, can only be justified if the signal's energy is very large at the receiver side. If low-power laser transmitter and electronics are desired, then one would seek a non-destructive signal detection method. That is, one in which the energy is not spent on measuring a non-matching dimension, but used directly on determining the component of interest.

In some cases, signal modulation using OAM may achieve higher spectral efficiency than OAM channel multiplexing if it is properly designed, as in the former an optimal selection of OAM modulation symbols may be found to overcome the effect of channel crosstalk, present in the latter [16]. This may be particularly true in laser communication systems propagating through turbulence, where the crosstalk produced at the receiver among adjacent or neighbor states can severely handicap detection. For instance, an OAM superposition taking only four active states at a time to form a modulation symbol from a set of eight total states could handle a throughput slightly more than 6 bits per channel use if all possible combinations are employed.

Among the methods to detect and decode superpositions of OAM states for data communications in free-space, we highlight the Mode Sorter [17] and the Shack-Hartmann sensor optimized for OAM detection [12]. These two sensors feature a theoretically high photon efficiency, as all the received optical signal is used for determining the active OAM components in the signal.

In this work we further study these two receiver architectures for the purpose of detecting and decoding multi-state OAM superpositions. These superpositions are designed to carry digital information in the form of signal modulation. We also propose the use of *OAM spectra* derived from the detected optical signals and evaluate the performance of the overall systems subject to the effects of turbulence. The decoding process consists of classifying the spectra (i.e., not images) using an algorithmic detector based on the symmetric Kullback-Leibler distance and a machine-learning classifier. Signal constellations using 16, 32, and 64 OAM symbols, delivering bit depths of 4, 5, and 6 bits are demonstrated.

The following section describes the optical design of each of these detectors, along with an OAM conjugate projection detector, used as the base case. It also defines the OAM spectra or OAM histograms used for signal classification. The optical simulation engine along with the parameter values for each detector and for the turbulence are provided in Section 3. Section 4 explains how the classification of symbols is carried out using the symmetric Kullback-Leibler distance. The performance achieved by each detector is described by the classification accuracy using confusion matrices for the three constellations studied. Section 5 summarizes our results and provides some discussion on the reach of these results.

2. Detector design

Given the fact that the OAM beam is a spatial mode, its topological charge composition can only be determined if the entire distribution of the beam is detected. This requirement could be relaxed if prior information about the beam is passed to the receiver, like the vortex' center or the angular section being detected. Such information is, however, unavailable in a communication link, particularly if the OAM-carrying beam is subject to atmospheric distortions. Thus, it is desirable to conceive a detector with which all spatial information available to the receiver is employed to determine the topological charge or the superposition thereof and to produce unbiased estimations if only partial information is available. We describe the two OAM-detecting architectures below, followed by the assumptions of the conjugate projection base case, that we denominate *conjugate projection (CP) detector*.

2.1. Optimized Shack-Hartmann detector

A Shack-Hartmann (SH) sensor is essentially composed of an array of identical microlenses followed by a detector array or imager placed at the focal plane of the lenses. A single optical

Optics EXPRESS

vortex can be detected by measuring the intensity spot displacement on each subaperture, caused by the phase gradient present in the vortex. Let $\mathbf{S}$ be the lateral displacement of the spot with respect to the center of the subaperture and $\nabla\Phi$ the phase gradient of the wavefront around the center. These quantities relate to each other as [12]

$$\mathbf{S} = S_x\,\hat{\mathbf{x}} + S_y\,\hat{\mathbf{y}} \approx \frac{f_{\mathrm{ml}}}{k}\nabla\Phi \tag{1}$$

where f_{ml} is the focal length of the microlens and k is the wave number. As described in Ref. [12], if a coaxial superposition of OAM states is carried by a beam, a more effective approach is to define a *local OAM map* at every pixel of the SH image, such that [12]

$$\hat{\ell}(x,y) = r(\nabla\Phi)\cdot\widehat{\upsilon} = \frac{k}{f_{\mathrm{ml}}}\mathbf{S}\cdot\widehat{\upsilon}\,r \tag{2}$$

where $r = |\mathbf{r}| = \sqrt{x_c^2 + y_c^2}$ is measured from the image center to the subaperture's center, and $\widehat{\upsilon}$ is a unitary vector perpendicular to the radial direction $\mathbf{r}$. For instance, if a single-state OAM mode is to be detected, a weighted average of $\hat{\ell}(x,y)$ over all pixels would deliver an accurate estimate of the beam's OAM state. Other methods of extracting the topological charge from a SH integrate along a circular contour. However, in the present work we aim to determine and classify superpositions of two or more OAM states, and thus propose the use of a local-OAM spectrum, defined as [12]

$$H_{\mathrm{SH}}(\ell,\rho) = \frac{\sum_{x,y}\rho(x,y)\delta_{\ell,\lfloor\hat{\ell}(x,y)\rceil}}{\sum_{x,y}\rho(x,y)} \tag{3}$$

as the input information of a classification decoder, described in Section 4. In Eq. (3), $\delta_{\ell,\lfloor\hat{\ell}(x,y)\rceil}$ is the Kronecker delta, with a non-zero value only for those pixels in which the nearest integer of $\hat{\ell}$ equals the integer ℓ. The weight function $\rho(x,y)$ is the intensity of the SH field or a monotonic function of it. The key feature is that Eq. (2) associates the local OAM map of the distorted wavefront to a one-dimensional local-OAM spectrum $H(\ell,\rho)$, as given in Eq. (3).

The described equations are based on discrete-valued spatial parameters due to the discrete nature of the SH detector. The resolution of the measurements will depend on the focal length f_{ml} of the microlens array, the pixel size of the imager, and the number of subapertures and pitch of the microlens array. These should be chosen to match the range of OAM states to be detected while allowing for an adequate OAM resolution. The details and the features of the OAM spectra are discussed in the following section. The Mode Sorter receiver is shown in branch (a) of Fig. 1 and the 8×8-subaperture SH sensor in branch (b).

2.2. Mode Sorter detector

The Mode Sorter (MS), proposed by Berkhout *et al.* [17], is a photon-efficient method for analyzing the topological charge of a beam using an optical geometric transformation followed by an imager, where the initially annular modes are projected as straight lines on a detector array, from which a local OAM spectrum can be produced.

The phase profile of the optical element that produces the geometrical transformation is given by [17]

$$\phi_1(x,y) = \frac{2\pi a}{\lambda f_{L_1}}\left[y\angle(x,y) - x\ln\left(\frac{\sqrt{x^2+y^2}}{b}\right) + x\right] \tag{4}$$

where λ is the beam's wavelength and f_{L_1} is the focal length of the far-field lens. The constants a and b are dimensional scaling parameters. The function $\angle(x,y) \in (-\pi,\pi]$ identifies the counterclockwise angle of the vector (x,y) from the positive x axis and has a discontinuity along

Optics EXPRESS

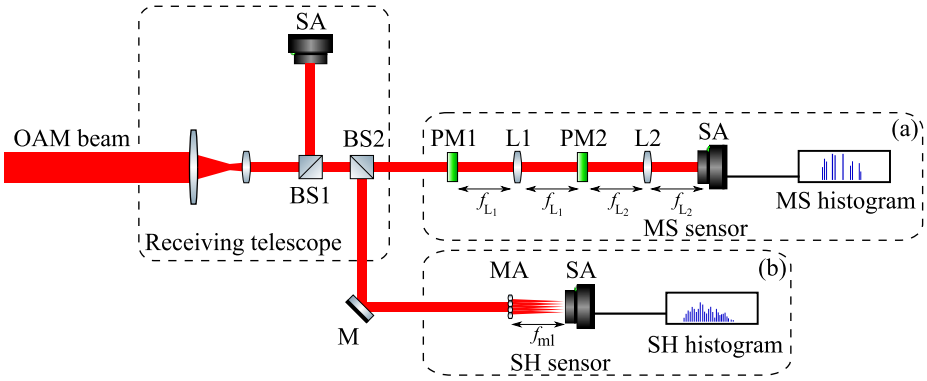

Fig. 1. Simulated optical assembly for sensing OAM superpositions using a Mode Sorter OAM receiver [branch (a)] and a Shack-Hartmann receiver [branch (b)]. Lenses are labeled L; BS are beam splitters; SA are sensor arrays; PM are discrete phase masks; MA is a microlens array.

the negative x axis. A phase correction ϕ_2 is required following the far-field transformation of ϕ_1, given by [17]

$$\phi_2(u,v) = -\frac{2\pi ab}{\lambda f_{L_2}} \exp\left(-u/a\right) \cos\left(v/a\right) \tag{5}$$

where (u, v) are the Cartesian coordinates of the Fourier plane of the lens. Spatial scaling at the output of the MS is also critical and must be adjusted to accommodate the range and resolution of OAM states to be analyzed. The component state analyzed appears as a straight segment of light at a transverse location on the imager. Its lateral displacement is defined by $\hat{y}_\ell = \left[\lambda f_{L_2}/(2\pi a)\right] \ell$. As reported in Ref. [17], there may be some ambiguity in determining the topological charge from the intensity lines, as their width caused by diffraction induces crosstalk in the measurement. Therefore, the scaling mentioned above and the adequate selection of OAM states need to be addressed in the performance analysis. In our numerical analysis we have simulated a full optical receiver based on spatial-light simulators (SLMs) that include all refraction and diffraction effects. The schematic for the simulated MS receiver is depicted in Fig. 1, on the upper branch, posterior to beam splitter BS2. This detector produces an OAM spectrum of the form

$$H_{\mathrm{MS}}(\ell, \rho) = \frac{\sum_{x,y} \rho(x,y) \delta_{y, \lfloor \hat{y}(\ell) \rceil}}{\sum_{x,y} \rho(x,y)}. \tag{6}$$

The weight function $\rho(x, y)$ is the intensity of the field, as in the SH case.

2.3. Conjugate projection detector

The topological charge analysis of a beam may be accomplished by projecting the electric field over each state within a set, also known as phase-flattening [18]. Our study includes a performance comparison with the conjugate projection (CP) detector, our base case, in which the received beam is analyzed by means of a phase screen, according to the scalar product

$$H_{\mathrm{CP}}(\ell, r) = \frac{|\sum_{x,y} \psi_r(x,y)^* \psi_\ell(x,y)|}{\sum_{x,y} |\psi_r(x,y)|^2} \tag{7}$$

where ψ_r is the discrete, conjugate of the received electric field and ψ_ℓ is the spatial phase of the OAM state ℓ. A possible experimental implementation would employ a spatial-light modulator (SLM), serving as an OAM scanning device sequentially programmed with every vortex phase

Optics EXPRESS

that is to be analyzed, followed by a converging lens whose focal plane could be recorded by sensor array. An example of this is offered in Ref. [19]. Similarly, a digital hologram may be prepared to identify the presence of up to 8 specified modes [2]. In our numerical comparison we specify a finite receive aperture and detector area, so that in the presence of turbulence, all refractive and diffraction effects are considered in the resulting spectra.

3. Simulations and generation of OAM spectra

The three detectors under study process the received wavefront in different ways, however they all need a detector array with which the intensity profile is sensed. Given the differences among the optical designs, it becomes necessary to establish a proper method for quantifying and comparing the performance of these detectors. For all three cases, we generate one-dimensional OAM spectra from the intensity image captured with the sensor array on each detector architecture.

The optical system in study comprises a transmitter capable of generating any combination of four coherently superimposed OAM states. Because the aim of this work is the study of the detection of OAM superpositions in the presence of turbulence, without loss of generality, we assume that the generated beams at the transmitter side have ideal Laguerre-Gauss (LG) distributions (with zero radial index) and that the superposition of the states is perfectly coherent. This is not a limiting factor, as any combination of OAM modes, coherent or incoherent, can in fact be detected with the proposed system.

The beam at the output pupil is assumed to have a fixed zero-order Gaussian radius of $w_0 = 1.5$ cm and exits through an aperture 10 cm in diameter, wide enough to sustain the near-field propagation of LG beams with ℓ up to ± 40 over 1 km. The beam waist is imposed to occur at the mid point of the propagation range. This range is sufficiently long to feature the various effects of turbulence in horizontal propagation near the ground.

The simulation engine runs in Python and includes the effect of turbulence by means of 8 to 16 phase screens (depending on the strength of the turbulence) evenly distributed along the path, generated according to the method described in Ref. [20]. These phase screens have been designed following the modified von Kármán spectrum, with outerscale $L_0 = 20$ m and innerscale $l_0 = 10$ mm [21]. The turbulence volume has 40 cm on a side with a resolution of 0.39 mm, corresponding to a discrete window of 1024×1024 pixels. Space periodicity in the phase screens is avoided by using sub-harmonic phase components. These also help increasing the effect of beam wander, which are usually under-represented in most simulations.

The receiver optics is common to all detectors studied here. It comprises a compressing telescope with an objective diameter of 20 cm and a compression ratio of 20×. The sensing area for both the SH detector and the MS detector is fixed to 10 mm on a side.

3.1. Simulation parameters for each detector

The SH detector uses 8×8 subapertures, each with 128×128 pixels. Each microlens has a focal length $f_{ml} = 65$ mm, which along with the other parameters has been chosen to let the system distinguish OAM states with $\Delta\ell \geq 2$ in the absence of turbulence while allowing a range of states up to $\ell = \pm 30$. The spectra for this detector are prepared according to Eq. (3).

The MS detector is designed with an intermediate lens L_1 with focal length $f_{L_1} = 20$ cm and the projecting lens L_2 with $f_{L_2} = 20$ cm as well. These lengths are chosen to guarantee an adequate spatial resolution and fit of the beam in the optical path, while keeping the effects of spherical aberration of the lenses low. In order to maintain an accurate numerical representation, particularly at the far field, an increase in resolution up to 4096×4096 was used at the plane of the detector array.

For the MS detector, the OAM spectra are created by integrating the intensity across a rectangle that encompasses the area corresponding to each OAM state. The dimensions of this rectangle

Optics EXPRESS

have been chosen to minimize crosstalk in the absence of turbulence. We conjecture that this selection also minimizes the crosstalk under turbulence.

The CP detector consists of imposing to the received field a conjugate vortex phase mask for each topological charge to be analyzed. The resulting field is propagated to the far field (by means of a converging lens), where it is sensed with an intensity detector array. The analyzing phase mask is centered and aligned with the turbulence-free optical path.

3.2. OAM signal modulation and generation of local OAM spectra

Encoding information in OAM symbols entails –at each symbol time– the selection of a small set of active OAM states from a larger set of predefined states. A symbol mapper groups the user bits and generates a unique symbol from the signal constellation [22]. This symbol activates the corresponding OAM states that comprise the superposition to be transmitted. Depending on the chosen architecture, this superposition may be coherent or incoherent. Given the binary nature of most communication systems, signal constellations usually contain 2^b symbols, where b is the bit depth of the constellation. In this work, we test 16-OAM, 32-OAM, and 64-OAM symbol constellations, which can carry (in an error-free channel) 4, 5, and 6 bits per channel use. We build an array of 70 possible OAM symbols using 4 active OAM states from a set of 8 states within the range $\ell \in [-20, 20]$ in intervals of $\Delta\ell = 5$. The superposition of 2, 3 and more topological charges is also possible, but not considered here. State $\ell = 0$ is not used, as it may serve for turbulence testing and other auxiliary services. From these permutations we can choose those symbols which render better performance, that is, lower probability of detection error. We later relate this choice with the classification method under evaluation.

Our simulations register all intensity and phase fluctuations at the pupil of the receiver. Apertures, lenses and mirrors are properly simulated using the Fresnel propagation method and correctly clip the fields, while ensuring proper management of the border effects within the propagation volume [20]. By looking at the entrance pupil of the receivers, one can see the significant distortion acquired by the beam, in some cases with only a general resemblance to the originally transmitted beam. In Fig. 2(a), we present an instance of the symbol OAM $(-20, -10, 10, 20)$ at the pupil of the receive telescope after a 1-km propagation under a turbulence strength defined by the refractive-index structure parameter value $C_n^2 = 3 \times 10^{-14}$ m$^{-2/3}$ using a zero-order beam diameter $w_0 = 1.5$ cm. Following the beam compression at the receiver, the intensity field produced at the SH detector' plane is displayed in Fig. 2(b), while Fig. 2(c) shows the intensity pattern at the focal plane of the MS detector. The images in Fig. 2(b)-(c) have been scaled for better representation. Single images for the CP detector are not meaningful, as it would require representations for all OAM states involved.

(a) (b) (c)

Fig. 2. OAM superposition (−20,−10,10,20) propagated over 1 km with $C_n^2 = 3 \times 10^{-14}$ m$^{-2/3}$: (a) Pupil plane; (b) Shack-Hartmann image. (c) Mode Sorter image.

Optics EXPRESS

A possible analysis of the effect of the turbulence on the beam superpositions is the evaluation of how distinguishable the distorted fields are from each other. To accomplish this we define three general scenarios according to their turbulence strength, measured by the Fried coherence parameter $r_0 = (0.423(2\pi/\lambda)^2 C_n^2 L)^{-3/5}$, where L is the propagation distance, C_n^2 is the refractive index structure parameter, and λ is the wavelength of the light.

The first scenario is labeled as "weak turbulence" for which $r_0 = 10$ cm (where $L = 1$ km, $\lambda = 850$ nm, and $C_n^2 = 2 \times 10^{-15}$ m$^{-2/3}$). We propagate each OAM superposition through 150 independent realizations of the turbulence, completing a total of 10,500 propagated instances. Each instance is detected using the receivers defined above to produce three OAM spectra, corresponding to SH, MS, and CP. The second simulated scenario is labeled "intermediate turbulence", for which $r_0 = 4$ cm, which corresponds to $C_n^2 = 9.2 \times 10^{-15}$ m$^{-2/3}$ and the same values for λ and L given above. As before, 150 independent propagation trials for each symbol were performed. The third and most challenging scenario is labeled "strong turbulence", with $r_0 = 2$ cm, corresponding to $C_n^2 = 2.9 \times 10^{-14}$ m$^{-2/3}$.

Some sample spectra produced by SH, MS, and CP detectors, corresponding to symbols $(-5, 5, 15, 20)$ and $(-20, -15, 5, 10)$ are shown in Fig. 3. The first row of spectra was obtained with $C_n^2 = 2\times10^{-15}$ m$^{-2/3}$, and the second row with $C_n^2 = 3\times10^{-14}$ m$^{-2/3}$. The OAM components are not easily identifiable by visual inspection, particularly in the SH spectra, but this is not a limitation, as it will be shown later.

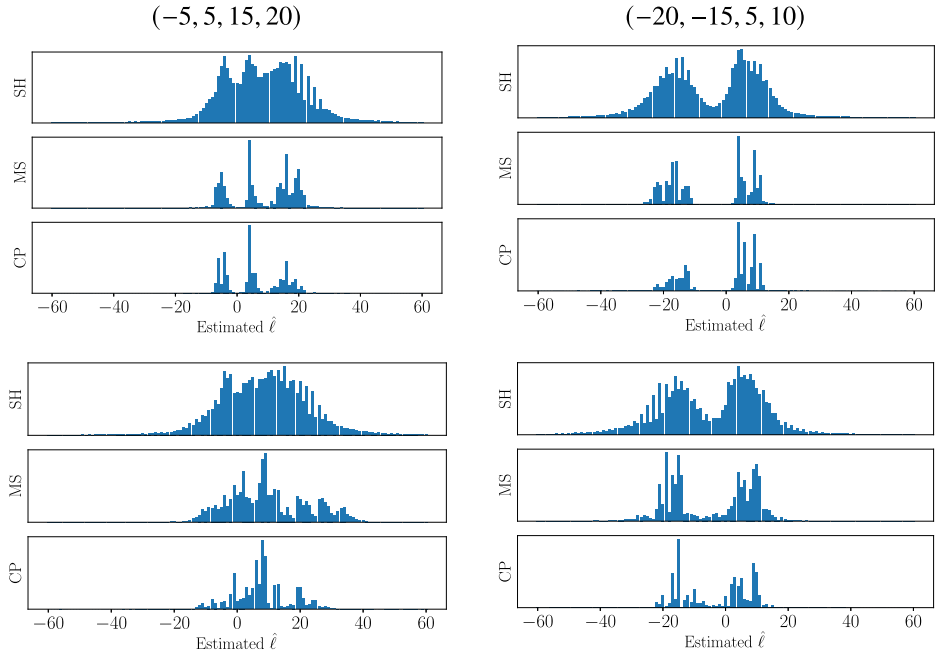

Fig. 3. OAM histograms for superpositions (−5,5,15,20) on first column and (−20,−15,5,10) on second column, propagated over 1 km with $C_n^2 = 2 \times 10^{-15}$ m$^{-2/3}$ (first row) and with $C_n^2 = 3 \times 10^{-14}$ m$^{-2/3}$ (second row) for Shack-Hartmann, Mode Sorter, and Conjugate Projection.

4. OAM symbol decoding

The definition of OAM spectrum can be used to distinguish symbol superpositions of two OAM states with accurate results, as reported in Ref. [12]. In the current work we extend this classification to symbols with 4 OAM states, without constraints on the balance of negative

Optics EXPRESS

and positive topological charges. We use the spectra in a supervised learning algorithm built to deliver the most likely symbol of the constellation. Because our objective is classifying symbols for an OAM-based signal modulation architecture, the identification of single OAM components is not required.

Some significant work has been recently proposed using machine-learning classification to detect optical fields, particularly from intensity images [19,23,24]. There are several classification algorithms that could be used for predicting the *class* to which a symbol belongs. For instance, Radial Basis Functions, K-Nearest Neighbors, Nearest Centroid, Decision Tree, and Support Vector Machine, all require a training phase using a small subset of *labeled* spectra, that is, distorted OAM spectra for which the symbols are known. These algorithms (available with Python package *scikit-learn* [25]) were tested and resulted in comparable performance under turbulence distortions. In our numerical setup, the quality of performance was not significantly affected by the method of classification, but instead by the optical detector architecture and its generated histograms, the strength of the turbulence, and the selection of OAM superpositions.

To quantify the distance between two OAM spectra we use the symmetric Kullback-Leibler (KL) divergence that measures the difference between two probability distributions. Unlike the non-symmetric KL divergence [26], the symmetric version delivers a unique scalar value that can be employed as a distance metric. Even though it does not satisfy the triangle inequality, in our application this does not imposes any limitation. The symmetric KL *distance* used herein is defined as [27]

$$D_{\mathrm{KL}}(H_1, H_2) = \sum_{\ell} H_1(\ell) \log_2 \left(\frac{H_1(\ell)}{H_2(\ell)} \right) + \sum_{\ell} H_2(\ell) \log_2 \left(\frac{H_2(\ell)}{H_1(\ell)} \right) \tag{8}$$

where $H_1(\ell)$ denotes OAM histogram 1 –for instance, as delivered by the detector– and $H_2(\ell)$ denotes OAM histogram 2 –for instance, one representing a class. In all cases, the spectra have been constrained within the range $\ell \in [-60, 60]$. A modification of the KL distance, the Jensen-Shannon divergence, could also be used for classification, but given that no observable changes were obtained in some preliminary classification results, we choose the symmetric KL for its simplicity.

4.1. Nearest centroid classification

The nearest centroid classification (NCC) method proved to be the most reliable among the three methods tested and also the fastest in training and testing (the others were K-Nearest Neighbors and Support Vector Machine, which showed similar performance but lower consistency). In the following we only present a description and results for this method. Testing possibly faster classification methods is out of the scope of this evaluation. NCC begins by determining a centroid for each symbol class. These centroids were built as the simple average of 50 local OAM spectra available within each class. A more geometric definition of centroid –as the minimizer of the sum of distances– could also be used. These 50 spectra make up the training set and were randomly chosen from the 150 instances available for each and every class.

NCC compares the histogram of each newly received symbol with the set of stored centroids using the symmetric KL distance. This implies a relatively low complexity, as only 2^b KL distance computations need to be solved for each received symbol. The NCC technique could be used with OAM spectra generated by any detector architecture, but mixing spectra from different detectors is not meaningful.

As shown in Fig. 4(a), the symmetric KL distance is effective in classifying symbols belonging to the same class (*intraclass* case in the Figure) and distinguish them from instances belonging to different classes (*interclass* in the Figure). Figure 4(b) shows how the instances of any given class are close to the their class' centroid but far away from the centroids of other classes. The results in this Figure are the aggregate performance for 64 classes from the SH detector affected

Optics EXPRESS

by intermediate turbulence. This supports the suitability of NCC to accomplish this task. Similar results were obtained for CP and MS detectors (not shown here). From this point on, we may use *class* instead of *symbol* as it is customary in the classification literature.

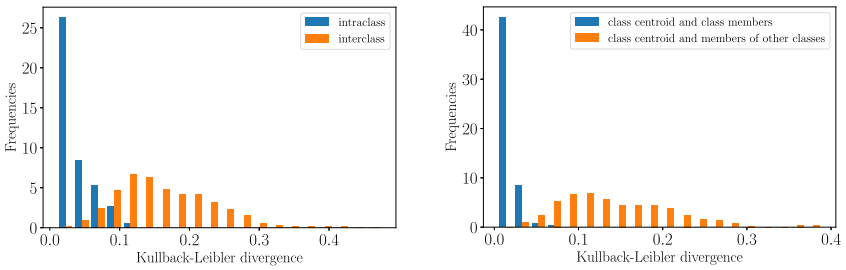

(a) (b)

Fig. 4. Test of the symmetric KL distance as a metric for symbol classification in intermediate turbulence. (a) Histogram of KL distances between elements within a class (blue) and between elements of different classes (orange). (b) Distances between a centroid and its class members (blue) compared to those between a centroid and other classes' members (orange). Both cases are for the SH detector and use all 70 classes.

A common way to represent the quality of the classification method is by means of a confusion matrix. In this matrix, both rows and columns represent the classes (or symbols): rows correspond to transmitted symbols and columns correspond to detected or predicted symbols. A perfect classification process will place all symbols on the diagonal of the confusion matrix. A detection error will be revealed as a marked square away from the matrix' diagonal. By definition, every element $C_{t,d}$ in the matrix C is equal to the number of observations known to be in class t (transmitted) and predicted to be in class d (detected). The classification accuracy is the fraction of the number of correct predictions $C_{t,t}$ with respect to the total number of predictions, that is,

$$\text{Acc} = \frac{\sum_t C_{t,t}}{\sum_{t,d} C_{t,d}}. \tag{9}$$

Accuracy is a good performance metric if one is working with a class-balanced data set, as it is the case, and can be used to determine the symbol error rate.

For an individual class one can compute the recall or true positive rate: $\text{Rec}(t) = C_{t,t}/\sum_d C_{t,d}$ and the precision or positive predictive value: $\text{Pre}(d) = C_{d,d}/\sum_t C_{t,d}$. Basically, the recall measures the concentration of a given row in the confusion matrix, and the precision measures the concentration of a given column. The conventional way to assess the concentration of both the row and the column associated with a given class is the F_1 score, defined as the harmonic mean between the precision and the recall of a specific class x, that is,

$$F_1(x) = 2\frac{\text{Pre}(x) \times \text{Rec}(x)}{\text{Pre}(x) + \text{Rec}(x)}. \tag{10}$$

This rate gives a measure of the contribution of a given class to the overall classification.

Our test showed that using seemingly stronger classification algorithms or enlarging the training set did not produce any noticeable improvement over the results from NCC. To produce more robust sets of symbols we followed two venues: reduce the number of classes and select these classes so they are more diverse. These two ways increase the *minimum distance* of the modulation format. The benefits of any changes can only be measured by setting up the classification framework and running it several times. These benefits will always depend on the

Optics EXPRESS

other classes used for classification. Thus, the selection of an optimum set of classes can be posed as a combinatorial optimization problem and is outside of the scope of the present work.

With that caveat, we propose a straightforward scheme for selecting a subset of classes from a large set of possible classes. For instance we could select 64 classes out of 70, or 32 classes out of 64, and so on. Based on the classification results using the complete set of 70 classes, we measure the classification quality associated with every single class using the F_1-score.

To show the effectiveness of the selection scheme based on the F_1 score in this case, we compare the classification accuracy of a constellation using randomly chosen symbols among the larger set. In Fig. 5(a), the accuracy of 32 randomly chosen symbols from the set of 64 in intermediate turbulence delivers accuracy values ranging from 0.94 to 0.97. This selection was repeated ten times to construct the histogram. Instead, the constellation composed of those 32 with the largest F_1 score delivers accuracy values from 0.97 to 0.99. Similarly, Fig. 5(b), the F_1-score selection of 16 symbols delivers accuracy values from 0.995 to 1.0, significantly better than the random selection. In the following section we present the classification results for constellations designed using F_1 score to prepare the constellation.

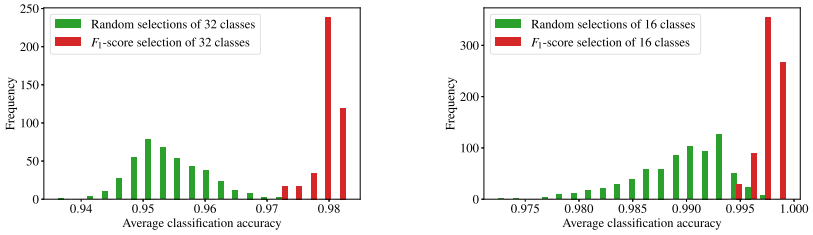

(a) (b)

Fig. 5. Histogram of the classification accuracy (effective detection) for (a) a selection of 32 classes chosen randomly among 64 classes (green) vs a selection according to the F_1 score (red). (b) Same comparison for 16-OAM out starting from 32-OAM.

4.2. Modulation performance for the 64-OAM constellation

The largest constellation with size 2^b one can construct using the 70 available superpositions is the 64-OAM constellation, conveying 6 bits per channel use. The selection of these 64 symbols is performed by rejecting those with the lowest F_1 score obtained in preliminary classification trials with 70 classes. This process also defines the classes to be used by the detection algorithm. Given that for each selected class 50 spectra are randomly picked as the training set, we test the detection algorithm using the 100 remaining spectra to populate the confusion matrix. To reach significant statistics on the system performance description, training and testing exercises are repeated by randomly selecting different sets of 50 symbols per class among the 150 available. This is done up to 20 times, so that up to $64 \times 100 \times 20 = 128000$ test trials can be in fact evaluated in the largest constellation. No additive noise is included in the detection process, equivalent to a system operating in high signal-to-noise ratio.

The confusion matrices for the 64-OAM modulation constellation are shown in Fig. 6, tested under weak turbulence (1st row of the Figure), intermediate turbulence (2nd row), and strong turbulence (3rd row). Detectors are organized in columns, where SH corresponds to the 1st column, MS to the 2nd column, and CP to the 3rd column. In each matrix, rows and columns were sorted by the average of the four OAM components that define each superposition, in ascending order. The first is $(-20, -15, -10, -5)$ and the last is $(5, 10, 15, 20)$. We omit the labels of the classes. To highlight the visual appearance of classification errors, we have removed the diagonal from all confusion matrices.

Optics EXPRESS

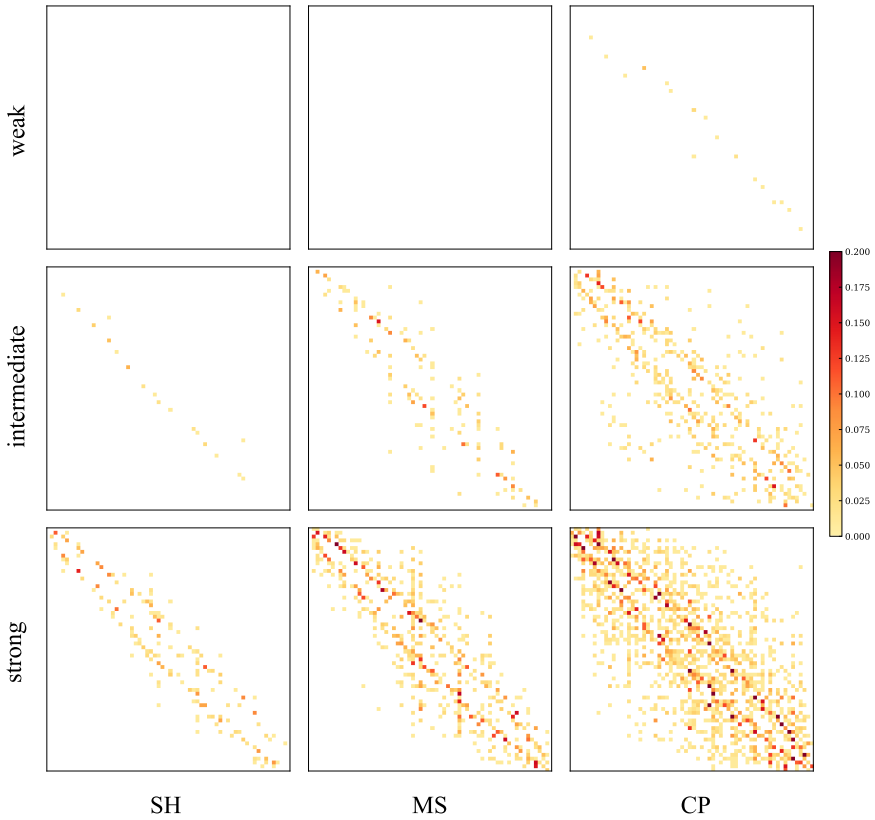

Fig. 6. Confusion matrices for the 64-OAM modulation constellation. Each matrix entails the detection of 128,000 symbols, using 20 different training sets. Turbulence strength is organized in rows, starting with the weak case. Columns represent SH, MS, and CP detectors from left to right. Diagonals have been removed. Events that occur more frequently are marked with a darker shade.

For the SH detector in weak turbulence [Fig. 6(a)], no errors occurred in the 128000 trials evaluated. Similarly, with the MS detector [Fig. 6(b)] there were only 4 errors for the same amount of trials, giving an accuracy of 0.99997. Evidently, in this benign setting, the number of trials would not be large enough for a bit-error rate characterization, but sufficient for the classification exercise. The least effective detector in this scenario is the CP detector, with 0.995 accuracy. That is, 99.5% of the detected symbols were correct using this classification method in weak turbulence, corresponding to 640 symbol detection errors out of 128000 combined tested events.

For intermediate turbulence, –second row in Fig. 6– the accuracy for SH is 0.994, with 768 detection errors; 0.949 for MS, with 6528 errors; 0.829 for CP, with 21888 errors. In strong turbulence the performance is much more severely affected. The accuracy for SH is 0.926, with 9472 detection errors; 0.746 for MS, with 106256 errors; and with a very low accuracy of 0.385 for CP, with 78720 errors. All these rates were obtained using 128000 trials.

These are outstanding performances for both the SH and the MS receivers using OAM spectra as the input of the classifier –which clearly outperform that of the CP detector in intermediate and stronger settings– and shows that transmission with OAM superpositions is feasible in turbulence channels with appropriate detectors. However, one may need to guarantee a more robust operation if intermediate and strong turbulence occur with higher frequency.

Optics EXPRESS

4.3. Modulation performance for the 32-OAM and 16-OAM constellations

We can increase the decoding strength to improve the detection accuracy of the algorithm at the cost of reducing the bit-depth of the symbol. This would in turn decrease the bit-error rate and/or gain in transmission distance. The choice of the 32-OAM signal constellation is done by ordering the classes according to their F_1 score obtained in strong turbulence and picking 32 with the highest. Given that OAM symbols use four active states within the ±20 range, one can transmit up to 5 bits per symbol. The results of the detection process for the 32-OAM constellation are shown in Fig. 7. In weak turbulence both the SH and MS detector show no errors (Acc = 1) after 64000 trials ($32 \times 20 \times 100$), where the CP delivers an accuracy of 0.999, with 64 errors.

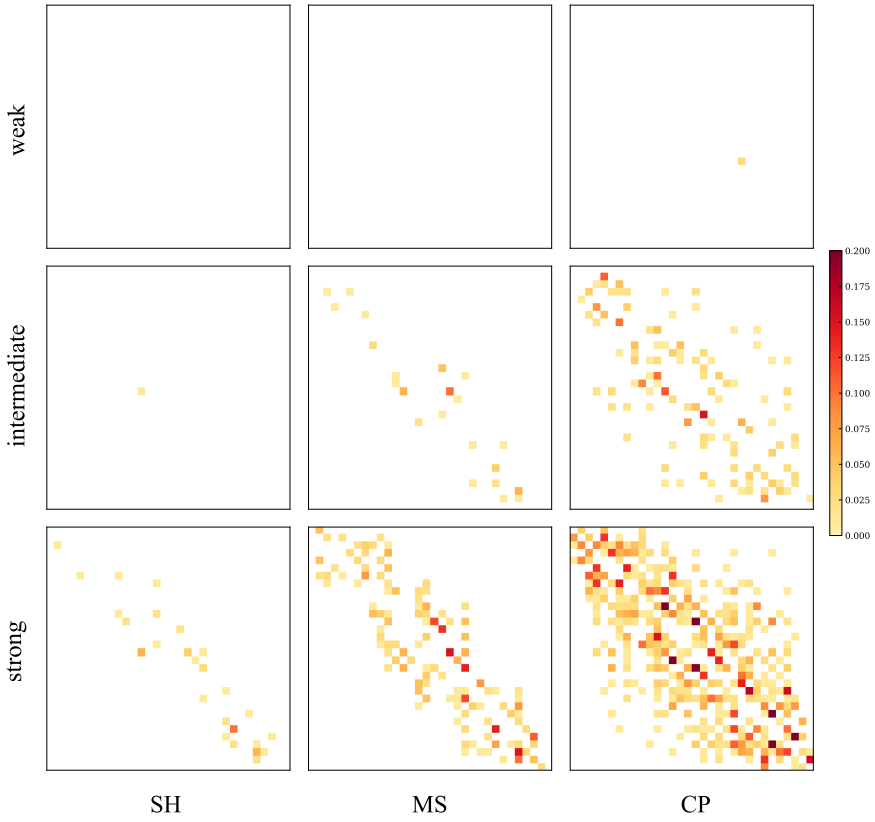

Fig. 7. Confusion matrices for the 32-OAM constellation. Each matrix entails the detection of 64,000 symbols. Turbulence strength is organized in rows and detector type in columns. Diagonals have been removed in all matrices.

In intermediate turbulence, –second row in Fig. 7– the accuracy improves to 0.999, 0.983, and 0.902 for SH, MS, and CP, respectively. In strong turbulence, Acc = 0.978, Acc = 0.868, and Acc = 0.561 for SH, MS, and CP, respectively. This is a very good classification result for SH, provided the complexity added by the turbulence to the OAM symbols.

If an even higher detection strength is needed, a 16-OAM signal constellation could also be chosen, in this case with a rate up to 4 bits per symbol. The results –obtained using 32000 trials– are shown in Fig. 8, where for the SH detector, accuracy values are 1.0 for weak and intermediate turbulence, and 0.997 for strong turbulence. The corresponding confusion matrices are shown on the first column of Fig. 8.

Optics EXPRESS

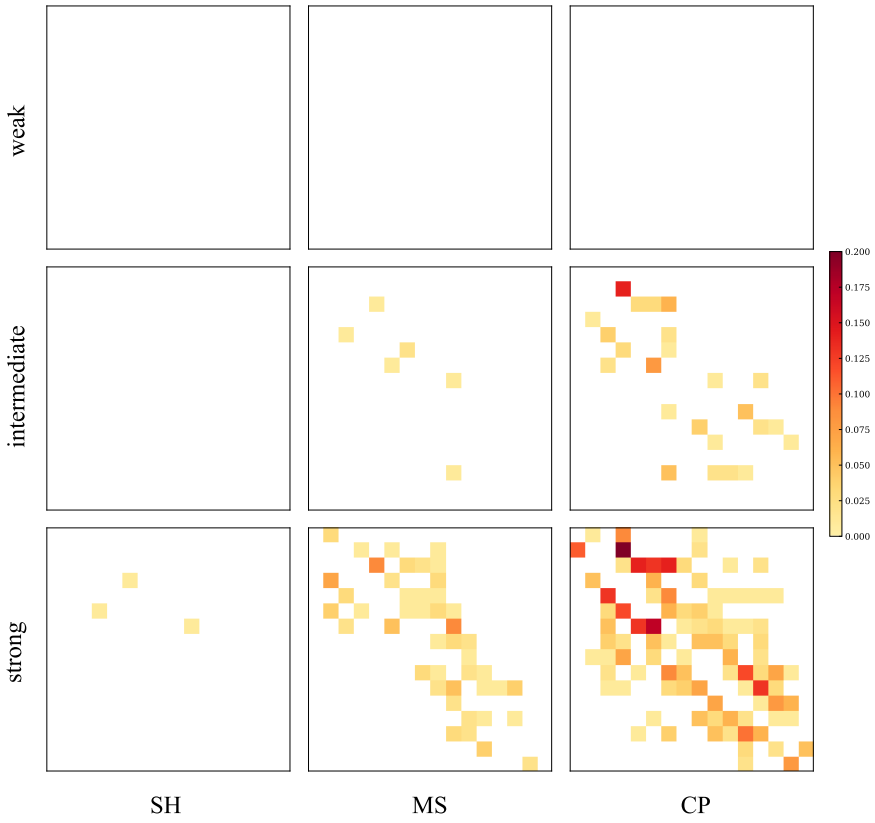

Fig. 8. Confusion matrices for the 16-OAM constellation. Each matrix entails the detection of 32,000 symbols. Turbulence strength is organized in rows and detector type in columns. Diagonals have been removed in all matrices.

The MS also delivers good accuracy rates: Acc = 1.0, Acc = 0.996, and Acc = 0.935 for weak, intermediate, and strong conditions, respectively. CP delivers 0.999 in weak turbulence, but even with this lower rate modulation constellation, it cannot deliver sufficiently good classification results in intermediate or stronger turbulence. All these results are summarized in Table 1.

Table 1. Detection accuracy for all OAM modulation constellations, 1-km propagation.

	64-OAM			32-OAM			16-OAM		
r_0	10 cm	4 cm	2 cm	10 cm	4 cm	2 cm	10 cm	4 cm	2 cm
Acc CP	0.995	0.829	0.385	0.999	0.902	0.561	0.999	0.954	0.732
Acc MS	0.99997	0.949	0.746	1.000	0.983	0.868	1.000	0.996	0.935
Acc SH	1.000	0.994	0.926	1.000	0.999	0.978	1.000	1.000	0.997
CC_{SH}	6.000	5.959	5.569	5.000	4.998	4.866	4.000	4.000	3.979

4.4. *Achieved capacity in turbulence*

We can calculate the effective channel capacity using a particular modulation constellation by means of the optimal probability P_t of sending symbol t over the turbulent channel. If $C_{t,d}$ is the average of element (t, d) in the confusion matrix, then, the channel capacity may be

Optics EXPRESS

estimated as [28]

$$\mathrm{CC} = \max_{P_t} \left(-\sum_t P_t \log_2(P_t) + \sum_t P_t \sum_d C_{t,d} \log_2(C_{t,d}) \right) \tag{11}$$

where all sums are bound by the cardinality N of the constellation. The capacity CC is calculated for all turbulence settings and modulation constellations and are bounded by their bit depth, namely, 6, 5, and 4 bits. These values correspond to the SH detector and are included in Table 1.

The classification method can also be applied to classes with mixed turbulence strengths, that is, including instances drawn from all simulated sets. This is desirable, as with non-controlled, real communication tests turbulence strength may change significantly within a few hours. We find that by creating classes using 450 OAM histograms per symbol (150 from each turbulence level), the classification algorithm shows improved performance with respect to the strong-turbulence case. This is shown in Fig. 9. In training and in testing and for each class, the three turbulence strengths were equally represented. In particular, an accuracy of $\mathrm{Acc_{SH}} = 0.999$, $\mathrm{Acc_{MS}} = 0.975$, and $\mathrm{Acc_{CP}} = 0.897$ are attained for the 16-OAM constellation. The confusion matrices for these results and those corresponding to the intermediate and strong turbulence scenarios are presented in Fig. 9.

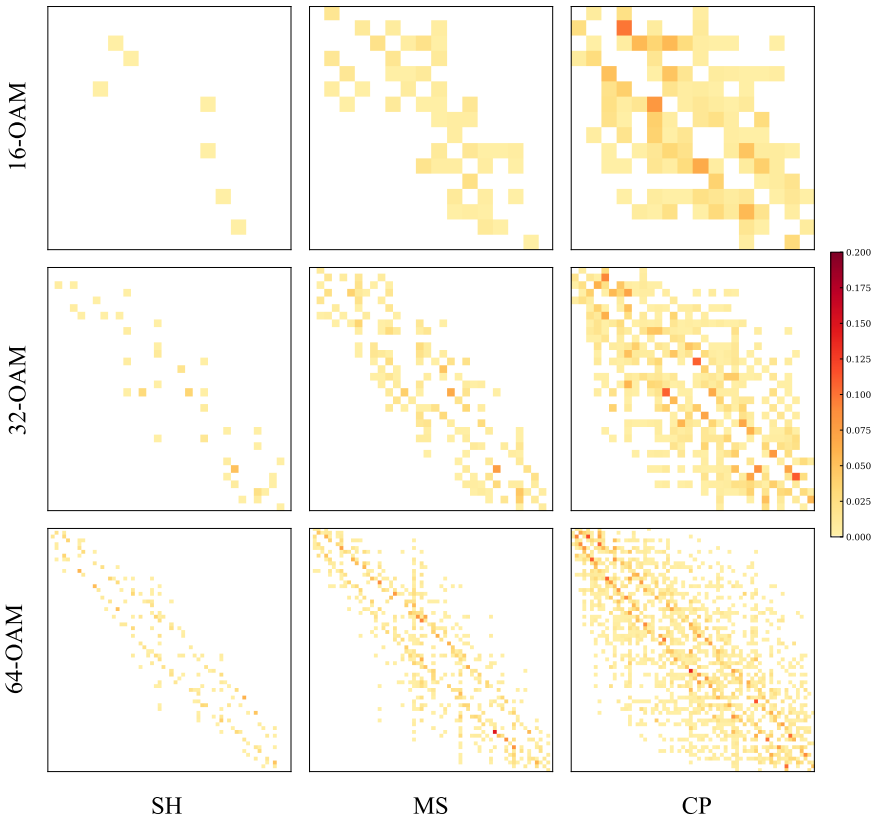

Fig. 9. Confusion matrices for the 64-OAM, 32-OAM, and 16-OAM constellations, tested with mixed turbulence conditions. Matrices with 64-OAM were obtained with 122880 symbols, those with 32-OAM were obtained with 61440 symbols, and matrices with 16-OAM were obtained with 30720 symbols. Turbulence strength is organized in rows and detector type in columns. Diagonals have been removed in all matrices.

Optics EXPRESS

5. Conclusion

In this work we have proposed the use of OAM-based modulation to increase the information throughput in a FSO communication link affected by turbulence. The detection of 16-OAM, 32-OAM, and 64-OAM signal constellations, based on the coherent superposition of four active OAM states from a set of eight is demonstrated by means of a realistic and accurate numerical propagation model. This method is tested on the optical Mode Sorter and on the Shack-Hartmann sensor, which are photon-efficient sensing architectures. The decoding method uses OAM spectra to reduce the dimensionality and, thus, the complexity of the detection process. Nevertheless, its performance is good in terms of the accuracy of classification and significantly overcomes the limitations imposed by beam wander and spatial distortions.

Our results show that both the Mode Sorter and the Shack-Hartmann sensors can deliver OAM spectra where the key features for discrimination are hidden, preserving relevant information about the components of the superpositions. In our simulations, the Shack-Hartmann wavefront sensor consistently achieved the best results. This advantage could be explained by the relatively large dynamic range of the SH sensor in terms of wavefront tilt and lateral displacement.

We found that good results can be obtained using OAM superpositions that are well separated according to the KL distance and trained with several turbulence strengths. Although the selection of the best set of symbols is a combinatorial optimization problem, high-accuracy detection can be achieved using a simple heuristic: selecting the classes based on their F_1 scores obtained in a classification experiment with a large set.

Funding. Agencia Nacional de Investigación y Desarrollo, Chile (Millennium Science Initiative Program ICN17-012, FR-1210297).

Disclosures. The authors declare no conflict of interest.

Data availability. Data underlying the results presented in this paper are not publicly available at this time but may be obtained from the authors upon reasonable request.

References

1. L. Allen, M. Beijersbergen, R. Spreeuw, and J. Woerdman, "Orbital angular momentum of light and the transformation of Laguerre-Gaussian laser modes," Phys. Rev. A **45**(11), 8185–8189 (1992).
2. G. Gibson, J. Courtial, M. J. Padgett, M. Vasnetsov, V. Pas'ko, S. M. Barnett, and S. Franke-Arnold, "Free-space information transfer using light beams carrying orbital angular momentum," Opt. Express **12**(22), 5448–5456 (2004).
3. M. Li, M. Cvijetic, Y. Takashima, and Z. Yu, "Evaluation of channel capacities of OAM-based FSO link with real-time wavefront correction by adaptive optics," Opt. Express **22**(25), 31337–31346 (2014).
4. T. Lei, M. Zhang, Y. Li, P. Jia, G. N. Liu, X. Xu, Z. Li, C. Min, J. Lin, C. Yu, H. Niu, and X. Yuan, "Massive individual orbital angular momentum channels for multiplexing enabled by Dammann gratings," Light: Sci. Appl. **4**(3), e257 (2015).
5. R. Gaffoglio, A. Cagliero, G. Vecchi, and F. P. Andriulli, "Vortex waves and channel capacity: Hopes and reality," IEEE Access **6**, 19814–19822 (2018).
6. G. Gbur and R. Tyson, "Vortex beam propagation through atmospheric turbulence and topological charge conservation," J. Opt. Soc. Am. A **25**(1), 225–230 (2008).
7. J. A. Anguita, M. A. Neifeld, and B. V. Vasic, "Turbulence-induced channel crosstalk in an orbital angular momentum-multiplexed free-space optical link," Appl. Opt. **47**(13), 2414–2429 (2008).
8. J. Wang, J.-Y. Yang, I. M. Fazal, N. Ahmed, Y. Yan, H. Huang, Y. Ren, Y. Yue, S. Dolinar, M. Tur, and A. E. Willner, "Terabit free-space data transmission employing orbital angular momentum multiplexing," Nat. Photonics **6**(7), 488–496 (2012).
9. M. Krenn, R. Fickler, M. Fink, J. Handsteiner, M. Malik, T. Scheidl, R. Ursin, and A. Zeilinger, "Communication with spatially modulated light through turbulent air across Vienna," New J. Phys. **16**(11), 113028 (2014).
10. T. Doster and A. Watnik, "Laguerre-Gauss and Bessel-Gauss beams propagation through turbulence: analysis of channel efficiency," Appl. Opt. **55**(36), 10239–10246 (2016).
11. B. Ndagano, I. Nape, M. A. Cox, C. Rosales-Guzman, and A. Forbes, "Creation and detection of vector vortex modes for classical and quantum communication," J. Lightwave Technol. **36**(2), 292–301 (2018).
12. J. Anguita and J. Cisternas, "Spatial-diversity detection of optical vortices for OAM signal modulation," Opt. Lett. **45**(19), 5534–5537 (2020).
13. R. Zambrini and S. M. Barnett, "Quasi-intrinsic angular momentum and the measurement of its spectrum," Phys. Rev. Lett. **96**(11), 113901 (2006).

Optics EXPRESS

14. J. Lin, X.-C. Yuan, M. Chen, and J. C. Dainty, "Application of orbital angular momentum to simultaneous determination of tilt and lateral displacement of a misaligned laser beam," J. Opt. Soc. Am. A **27**(10), 2337–2343 (2010).
15. Y. Li, K. Morgan, W. Li, J. K. Miller, R. Watkins, and E. G. Johnson, "Multi-dimensional QAM equivalent constellation using coherently coupled orbital angular momentum (OAM) modes in optical communication," Opt. Express **26**(23), 30969–30977 (2018).
16. I. B. Djordjevic and M. Arabaci, "LDPC-coded orbital angular momentum (OAM) modulation for free-space optical communication," Opt. Express **18**(24), 24722–24728 (2010).
17. G. Berkhout, M. Lavery, J. Courtial, M. Beijersbergen, and M. Padgett, "Efficient sorting of orbital angular momentum states of light," Phys. Rev. Lett. **105**(15), 153601 (2010).
18. H. Qassim, F. M. Miatto, J. P. Torres, M. J. Padgett, E. Karimi, and R. W. Boyd, "Limitations to the determination of a Laguerre-Gauss spectrum via projective, phase-flattening measurement," J. Opt. Soc. Am. B **31**(6), A20–A23 (2014).
19. T. Doster and A. T. Watnik, "Machine learning approach to OAM beam demultiplexing via convolutional neural networks," Appl. Opt. **56**(12), 3386–3396 (2017).
20. J. D. Schmidt, *Numerical Simulation of Optical Wave Propagation with Examples in MATLAB* (SPIE, United States, 2010).
21. R. Lane, A. Glindemann, and J. Dainty, "Simulation of a Kolmogorov phase screen," Waves Rand. Media **2**(3), 209–224 (1992).
22. I. B. Djordjevic, J. A. Anguita, and B. Vasic, "Error-correction coded orbital-angular-momentum modulation for FSO channels affected by turbulence," J. Lightwave Technol. **30**(17), 2846–2852 (2012).
23. S. R. Park, L. Cattell, J. M. Nichols, A. Watnik, T. Doster, and G. K. Rohde, "De-multiplexing vortex modes in optical communications using transport-based pattern recognition," Opt. Express **26**(4), 4004–4022 (2018).
24. T. Giordani, A. Suprano, E. Polino, F. Acanfora, L. Innocenti, A. Ferraro, M. Paternostro, N. Spagnolo, and F. Sciarrino, "Machine learning-based classification of vector vortex beams," Phys. Rev. Lett. **124**(16), 160401 (2020).
25. F. Pedregosa, G. Varoquaux, A. Gramfort, V. Michel, B. Thirion, O. Grisel, M. Blondel, P. Prettenhofer, R. Weiss, V. Dubourg, J. Vanderplas, A. Passos, D. Cournapeau, M. Brucher, M. Perrot, and E. Duchesnay, "Scikit-learn: Machine learning in Python," Journal of Machine Learning Research **12**, 2825–2830 (2011).
26. D. J. MacKay, *Information Theory, Inference and Learning Algorithms* (Cambridge University, 2003).
27. S. Kullback and R. Leibler, "On information and sufficiency," Ann. Math. Stat. **22**(1), 79–86 (1951).
28. M. Malik, M. O'Sullivan, B. Rodenburg, M. Mirhosseini, J. Leach, M. P. J. Lavery, M. J. Padgett, and R. W. Boyd, "Influence of atmospheric turbulence on optical communications using orbital angular momentum for encoding," Opt. Express **20**(12), 13195–13200 (2012).